1 **The annotation and analysis of complex 3D plant organs using**

2 **3DCoordX**

3

4 Athul Vijayan[1,#a,¶], Soeren Strauss[2,¶], Rachele Tofanelli[1], Tejasvinee Atul Mody[1], Karen

5 Lee[3], Miltos Tsiantis[2], Richard S. Smith[2,3] and Kay Schneitz[1,*]

6 [1]Plant Developmental Biology, TUM School of Life Sciences, Technical University of

7 Munich, Freising, Germany

8 [2]Department of Comparative Developmental and Genetics, Max Planck Institute for Plant

9 Breeding Research, Cologne, Germany

10 [3]The John Innes Centre, Norwich Research Park, Norwich, United Kingdom

11 [#a]Current address

12 Department of Comparative Developmental and Genetics, Max Planck Institute for Plant

13 Breeding Research, Cologne, Germany

14

15 [*]Corresponding author

16 Email: kay.schneitz@tum.de (KS)

17

18 [¶]These authors contributed equally to this work.

19

20 Short title: Computational cell annotation in 3D digital plant organs

21

22 Email addresses authors:

23 Athul Vijayan: avijayan@mpipz.mpg.de

24 Soeren Strauss: strauss@mpipz.mpg.de

25 Rachele Tofanelli: r.tofanelli@tum.de

26 Tejasvinee Atul Mody: t.mody@tum.de

27 Karen Lee: karen.lee@jic.ac.uk

28 Miltos Tsiantis: tsiantis@mpipz.mpg.de

29 Richard Smith: Richard.Smith@jic.ac.uk

30 Kay Schneitz: kay.schneitz@tum.de

31

32

33

Abstract

A fundamental question in biology concerns how molecular and cellular processes become integrated during morphogenesis. In plants, characterization of 3D digital representations of organs at single-cell resolution represents a promising approach to addressing this problem. A major challenge is to provide organ-centric spatial context to cells of an organ. We developed several general rules for the annotation of cell position and embodied them in 3DCoordX, a user-interactive computer toolbox implemented in the open-source software MorphoGraphX. It enables rapid spatial annotation of cells even in highly curved biological shapes. With the help of 3DCoordX we obtained new insight by analyzing cellular growth patterns in organs of several species. For example, the data indicated the presence of a basal cell proliferation zone in the ovule primordium of *Arabidopsis thaliana*. Proof-of-concept analyses suggested a preferential increase in cell length associated with neck elongation in the archegonium of *Marchantia polymorpha* and variations in cell volume linked to central morphogenetic features of a trap of the carnivorous plant *Utricularia gibba*. Our work demonstrates the broad applicability of the developed strategies as they provide organ-centric spatial context to cellular features in plant organs of diverse shape complexity.

Introduction

It remains a salient challenge to understand the generation of biological shape. Gaining comprehensive insight into the multi-scale processes underlying morphogenesis critically depends on the quantitative description of molecular, cellular, and tissue-level parameters, such as gene and protein expression, cell geometry, and cell topology

57 [1–6]. Moreover, as prominently proposed by D'Arcy Thompson, the generation of shape

58 can be achieved by growth that is oriented relative to a coordinate system imposed on the

59 organ [7]. Thus, insight into tissue morphogenesis further relies on putting cellular data

60 into context by placing them within an organ-related frame of reference [8–11].

61

62 Realistic 3D digital organs with cellular resolution have become indispensable tools for

63 the study of morphogenesis. They can be obtained by deep imaging of fluorescently

64 marked specimens using for example confocal laser scanning microscopy (CLSM) or

65 light sheet fluorescence microscopy (LSFM) followed by 3D cell segmentation of the

66 obtained z-stacks of optical sections with the help of constantly improving software [11–

67 17]. Tissues and organs of model plants are particularly well suited for the generation of

68 such 3D digital representations. Plant cells are immobile simplifying the detection of

69 cellular growth patterns associated with tissue formation. In addition, plant tissues are

70 characterized by a small number of different cell types and often exhibit a well-structured,

71 layered organization. Thus, they usually feature a cellular anatomy of manageable

72 complexity. Accordingly, a growing number of realistic 3D digital tissues with cellular

73 resolution are being generated, mainly in the model plant *Arabidopsis thaliana* [9,10,18–

74 27].

75

76 With the help of 3D digital organs quantitative information about geometric and

77 molecular parameters of up to thousands of cells can readily be obtained using open-

78 source software, such as MorphoGraphX [11,14] (preprint). However, meaningful

79 exploration of such complex data sets remains challenging. In particular, it is important to

80 provide spatial context by placing the cell's data within an organ-related frame of

81 reference [8]. Several computational pipelines have been established that provide such a

82   tissue-level frame of reference and allow the semi-automatic annotation of 3D cellular

83   properties in a plant tissue context with cellular resolution: iRoCS [9], 3DCellAtlas [10],

84   and 3DCellAtlas Meristem [22]. These computational pipelines have been applied very

85   successfully for the annotation of cells and tissues in the main root and the hypocotyl,

86   radially symmetric organs with limited curvature, or the SAM, a dome-shaped structure

87   exhibiting an anatomy of moderate complexity. However, not all plant organs fall into

88   these simple morphogenetic categories. For example, strong curvature caused by

89   developmentally regulated differential growth limits the usefulness of the implemented

90   analytical strategies in iRoCS and 3DCellAtlas, particularly for indexing the axial

91   position of a cell and determining its absolute distance to a reference. Yet, curvature

92   represents a central element of the morphogenesis of plant organs with complex 3D

93   shapes [28]. Many plant organs exhibit varying degrees of curvature, for example the

94   apical hook of seedlings, leaves, or floral organs, such as sepals or petals. The ovule, the

95   major female reproductive organ in higher plants, constitutes a particularly prominent

96   example. Ovules are characterized by complex anatomy consisting of a central "trunk",

97   made up of several functionally distinct tissues stacked on top of each other, and by one

98   or two laterally attached integuments, determinate planar tissues that eventually develop

99   into the seed coat [29]. Moreover, most angiosperm ovules exhibit an extreme curvature

100   due to asymmetric growth of the integuments [30].

101

102   Here, we used the ovule of *Arabidopsis thaliana* as a model to develop new generic

103   strategies, implemented in MorphoGraphX, that allow the straightforward establishment

104   of intrinsic coordinate systems in organs of simple or elaborate shapes. To this end we

105   took advantage of a recently generated digital 3D reference atlas of ovule development in

106   Arabidopsis [27]. We illustrate how such a coordinate system enables rapid annotation of

107   cell identity and cell position in 3D and greatly facilitates the quantitative analysis of

108   cellular features. We applied our strategies to an investigation of cell proliferation

109   patterns in the ovule primordium and the cellular basis of differential integument growth.

110   Finally, we demonstrate the broad applicability of the introduced concepts by providing

111   proof-of-concept analysis for selected parameters in different plant organs of varying

112   shape complexity.

113

Results

Curvature-related complications in the assignment of axial position

117   The analytical strategies for the positional annotation of individual cells relative to tissue

118   organization depend on the structure under study. For example, the straightforward

119   approaches employed in iRoCS and 3DCellAtlas involve cylinder coordinates and work

120   very well for indexing axial position of cells relative to a reference in the root or

121   hypocotyl, structures exhibiting limited curvature (Fig. 1A). However, asymmetric

122   growth caused by differential cell proliferation and/or cell expansion can result in slanted

123   or highly curved organs. In these instances, such approaches may lead to cells of the same

124   indexed position having different absolute axial distances to a common reference (Fig.

125   1B). Thus, we devised a different strategy to minimize such axial distance errors when

126   assigning 3D positional annotation to cells of organs that exhibit complex shapes. Our

127   approach takes cues from central patterning events that frequently occur during early

128   plant organogenesis, in particular the distinction of radial layers, the subdivision into

129   anterior-posterior domains, and the establishment of a proximal-distal (axial) distance

130   field (Fig. 1C,D). The proximal-distal distance of a cell relative to a user-defined

131 reference is estimated by finding the shortest path through the cell centroids. Importantly,

132 the search is confined to a given tissue layer and may not cross the anterior-posterior

133 domain. The restriction to a tissue layer removes a large part of the axial distance error as

134 the shortest path through the tissue layers cannot extend through interior tissues (Fig. 1C).

135 On top of this restriction, prohibiting the shortest path from passing the anterior-posterior

136 boundary further minimizes the error (Fig. 1D).

137

Development of the Arabidopsis ovule

139 The typical angiosperm ovule represents a prime example of an elaborately curved

140 structure. Ovule development in *Arabidopsis thaliana* is well described [24,27,31,32]

141 (Fig. 2A,B). During stage 1 the ovule emerges as a finger-like protrusion from the

142 placenta (staging according to [27,32]). Eventually, three elements can eventually be

143 recognized along the trunk of the developing ovule: the nucellus at its tip, the chalaza in

144 the center, and the funiculus at the bottom. The nucellus generates the large sub-

145 epidermal megaspore mother cell (MMC) that will undergo meiosis during stage 2.

146 During stage 3 one of the meiotic products eventually develops into the haploid embryo

147 sac or female gametophyte carrying the egg cell proper. The chalaza is characterized by

148 two epidermally-derived integuments, lateral tissues that initiate from its flanks during

149 stage 2. The outer integument represents a bilayered structure while the inner integument

150 eventually consists of three cell layers. The two integuments grow around the nucellus but

151 leave open a small cleft, the micropyle, through which the pollen tube can reach the

152 embryo sac. The funiculus, a stalk-like structure, harbors the vascular strand and connects

153 the ovule to the placenta. The mature Arabidopsis ovule features an elaborately curved

154 shape. Curvature is caused in part by the integuments bending around the nucellus during

155 stage 3 until their tips eventually locate next to the funiculus (anatropy). In addition, the

156   funiculus forms a bend as well. Overall, the mature ovule exhibits a characteristic doubly-

157   curved structure (Fig. 2A).

158

159   Developmental axes of the ovule primordium

160   The Arabidopsis ovule primordium exhibits the typical radial organization into the L1,

161   L2, and L3 cell layers [33,34]. In addition, the distal nucellus, central chalaza, and

162   proximal funiculus, represent three proximal-distal pattern elements along the trunk of the

163   developing ovule. Gene expression patterns underlying the proximal-distal organization

164   of the primordium are relatively well understood [27,35,36]. Importantly, the early

165   primordium is not growing in a straight fashion but rapidly adopts a slant relative to the

166   placenta surface, with the small angle of the slant facing the septum. It represents the first

167   morphological sign of an anterior-posterior polarity (Fig. 1C,D) [27]. The presence of an

168   anterior-posterior axis is further supported by the anterior expression of the class III HD-

169   ZIP gene *PHABULOSA* in the early primordium [37]. To corroborate the establishment of

170   an anterior-posterior axis in the stage 1-I ovule primordium we investigated the spatial

171   signal distribution of pKAN1::KAN1:2xGFP, a reporter for *KANADI1* expression [38].

172   We observed detectable signal exclusively in the epidermis of the posterior ovule

173   primordium (Fig. 2C). Interestingly, we did not detect expression in the tip of the

174   primordium. By stage 2-I reporter signal appeared to be restricted to the posterior

175   epidermis of the prospective funiculus.

176

177   In summary, the combined evidence strongly suggests the establishment of a radial, a

178   proximal-distal, and an anterior-posterior axis in the ovule primordium. At the same time,

179   the slant represents an early morphological manifestation of the ovule becoming a curved

180   structure.

181

Cell layer detection, individual organ separation, and anterior-posterior domain annotation in 3D

184 The annotation of cell position in 3D in the slanted ovule primordium required the

185 application of the general principles outlined above. To be able to do so in a fast and

186 robust manner we devised a new method for radial tissue labeling. Current pipelines, such

187 as 3DCellAtlas and 3DCellAtlas Meristem, invoke a surface mesh as a central tool for

188 cell and tissue annotation in the root, hypocotyl, and the SAM [10,22]. However,

189 establishing a surface mesh does not work well in situations where organs are in close

190 contact with each other as is often the case for young ovule primordia attached to the

191 placenta (Fig. 3A). The resulting individual surface meshes fail to outline the surfaces of

192 the cells in contact and it is labour intensive to recreate a surface mesh in such instances.

193

194 To address this problem, we developed a new strategy to perform automatic layer

195 detection that groups cells into L1, L2, and L3 without a need for a surface mesh (Fig.

196 3A-C). In a first step L1 cells are clustered on the basis of a cell at the outer surface of the

197 organ not being flanked by a neighboring cell at their outer surface. This feature is

198 captured by defining the ratio of unshared wall area to shared wall area of individual cells

199 (outside wall area ratio). Once L1 cells are clustered, L2 and L3 cells are found by their

200 relative distances to the L1 cells. To this end a network of cell centroids is established and

201 the shortest number of centroids a cell must cross to reach to the nearest L1 cell is

202 determined. The corresponding result essentially reveals how many cells separate the cell

203 of interest from the L1. The information can be directly used to cluster cells into L2 and

204 L3 as L2 cells are direct neighbors of L1 cells and L3 cells are separated from the L1 by

205 more than one cell. The strategy does not completely solve the issue when surface cells of

8

206 neighboring organs are in full contact. However, the process works well when there is

207 partial contact that still leaves behind a significant outside unshared cell wall area. This

208 approach successfully annotated the radial tissue layers in ovule primordium or the shoot

209 apical meristem (Fig. 3A-C, Fig S1).

210

211 Another problem relates to the separation of the multiple ovule primordia attached to the

212 placenta into distinct units to allow ovule-specific analyses. We devised a method that

213 takes advantage of the cell connectivity graph (Fig. 3D). From a selected cell at the distal

214 end on each different ovule, distances to all other cells on the cell connectivity graph are

215 computed. Cells are then assigned a label based on their nearest selected cell on that

216 graph. A further parameter sets a maximum size of the ovules (in number of cells from

217 the selected cells) to separate the ovules from their surrounding tissue. To facilitate

218 downstream analysis, different labeling types, such as the cell layers and the ovule labels,

219 are combined to create a unique label for each layer in every ovule.

220

221 In the last step, cells of anterior and posterior domains of about similar dimensions are

222 obtained by manual selection (Fig. 3E). For the funiculus we also devised a semi-

223 automatic method to distinguish the anterior and posterior domains (Fig. S2). In

224 summary, the outlined approaches enable the generation of 3D digital ovule primordia of

225 separate identities and near-perfect radial and anterior-posterior tissue annotation with

226 minimal user input.

227

228 **Assignment of proximal-distal position to individual cells in 3D**

229 To determine the proximal-distal (axial) position of an ovule primordium cell we

230 generated a method that applies to 3D digital ovules for which radial cell layers and the

231   anterior-posterior domains have already been annotated. The proximal-distal position of

232   each cell is calculated, either in terms of cell index or absolute or relative distance to a

233   reference, in a two-step procedure (Fig. 3F,G). In the first step, a Bezier ring (a

234   mathematically defined curved line) will serve as reference for the proximal-distal

235   distance field and is placed at one end of the tissue. In the case of the cone-shaped ovule

236   primordium a small, near point-size Bezier ring is positioned at the distal tip of the

237   primordium. Positioning the Bezier ring at the distal tip correlates with a biologically

238   relevant maximum of the phytohormone auxin at the tip as inferred from the expression

239   of the auxin response reporter pDR5::GFP [39], the spatial signal of the auxin sensor

240   R2D2 [40,41], and the finding that polar auxin transport mediated by *PINFORMED1*

241   (*PIN1*) is required for ovule primordium formation [42,43]. In case of the mature

242   funiculus that is close in shape to a curved cylinder, a larger Bezier ring is placed at its

243   proximal end. Origin cells are then defined by their close distance in 3D (usually 5-15

244   μm) to the user-specified Bezier ring (Fig. 1C,D). They act as seeds for the distance

245   coordinates of the remaining cells of the tissue that are obtained by searching for the

246   shortest path through the cell centroids to the centroid of an origin cell. The search is

247   restricted to a radial layer and by the anterior-posterior boundary. It should be noted that

248   with this approach small axial distance errors still occur within the anterior or posterior

249   domains depending on the number of laterally arranged cell files within these areas. The

250   remaining errors are typically in the range of a few microns, but can be eliminated when

251   taking individual cell files into account. This is possible within the software, however, the

252   procedure involves cumbersome manual annotation of all cell files for each cell layer.

253   Moreover, the gain of resolution is minimal.

254

255   **A coordinate system for integuments**

256   The two integuments undergo complex morphogenesis with the inner integument

257   eventually resembling a curved cylindrical shell and the outer integument developing into

258   a curved hood-like shell (Fig. 2A,B,F). Both integuments are characterized by their own

259   intrinsic developmental axes (Fig. 2E-H). A distinct adaxial-abaxial (dorso-ventral) axis

260   is prominent as the individual cell layers differ in cellular morphology and gene

261   expression patterns [32,37,44–46] (Fig. 2E). Both integuments also feature their own

262   proximal-distal axes (Fig. 2A,F). Related to its hood-like shape the outer integument

263   flanks a frontal section and features a medial-lateral axis (Fig. 2G). As a rule, we position

264   the ovule with the anterior domain and the micropyle pointing to the left and the proximal

265   end of the funiculus pointing towards the bottom right. Based on this arrangement we

266   define the left and right lateral sides of the medial-lateral axis (Fig. 2H).

267

268   We successfully applied to the integuments some of the same formal strategies as

269   described for the primordium or funiculus. In an initial step, the integumentary adaxial-

270   abaxial cell layers are labelled manually. In a subsequent step, medial-lateral coordinates

271   of all cells of a given integument layer are established relative to a file of posterior

272   midline cells (Fig. 4A). Cell distance is computed in terms of how many cells separate a

273   given cell from the midline (Fig. 4B). Cells along the medial-lateral axis can be grouped

274   further into median and lateral subdomains that occupy about half the width of an

275   integument layer. For example, for the outer layer of the outer integument we grouped

276   cells that are located three cells to the left or right of the posterior midline cells into the

277   median domain. The remaining cells are classified as lateral cells (Fig. 4C). In the

278   following step, proximal-distal distance coordinates are assigned for all integument cells.

279   A Bezier ring is first placed at the proximal end of the inner side of the outer integument

280   (next to its inner layer) facing the outer layer of the inner integument (Fig. 4D). The

281 circular origin is in the same plane as the ring-shaped expression pattern of the

282 pCUC3::CUC3:CFP reporter which marks the proximal base of the two innermost layers

283 of the inner integument, respectively (Fig. 4E). Members of the CUC gene family are

284 generally required for primordium initiation and organ boundary formation [43,47–52].

285 Origin cells are then defined by their close user-specified distance to the Bezier ring in

286 3D (about 5-15 μm). As a direct result of the placement of the Bezier ring cells of the

287 outer layer of the outer integument that are in direct contact with the subepidermal

288 proximal chalaza are assigned a negative value for the proximal-distal position (Fig. 4F).

289 This feature can be used to separately cluster and analyze those cells. Finally, proximal-

290 distal distance coordinates of the integument cells are obtained by searching for the

291 shortest path through the cell centroids to the centroid of an origin cell (Fig. 4F,G). The

292 search is again restricted to a given tissue layer and may not cross the medial-lateral

293 boundary. Taken together, the procedure assigns medial-lateral and proximal-distal

294 positions for all cells of the integuments.

295

Differential distribution of cellular growth patterns during

early ovule development

298 To provide proof of concept for the usefulness of our computational tools in the

299 quantitative analysis of cellular patterns in a 3D context we assessed spatial growth

300 patterns in selected aspects of ovule development. To this end we made use of a

301 previously published dataset of wild-type 3D digital ovules of the Col-0 accession [27].

302 We first focused on primordium outgrowth. It was previously shown that ovule primordia

303 grow in a continuous fashion based on an analysis of the total number of cells and the

304 increase of organ volume from stages 1-I to 2-I [24,27]. However, it remained unclear

305 how cell numbers and cell volumes of the radial layers compare to each other. In addition,

12

306   it was not known if mitoses are randomly distributed along the proximal-distal axis or if

307   they preferentially occur in specific domains. To address these questions we analyzed 52

308   3D digital wild-type ovule primordia that encompassed stages 1-I to 2-I (Fig. 5A,B).

309

310   We initially undertook a comparison of cell volumes between stages (Fig.5C) and radial

311   layers (Fig. 5D) (Table 1). In this dataset the L2-derived MMCs at stage2-I feature an

312   average cell volume of 543.3 μm^3 ± 120.6 μm^3 (mean ± SD) with a minimal volume of

313   335 μm^3 [27]. Thus, the volume of the MMCs is beyond the largest cell volumes

314   observed for other cells (Fig. 5C). We therefore eliminated the MMCs from this analysis

315   to eliminate skewing of the results due to their out-of-range size. We observed that the

316   average volume of L1 cells slightly increased during development while the average

317   volume of L2/L3 cells stayed about constant (Fig. 5D) (Table 1). The results further

318   indicated that with the exception of the MMCs the L2 and L3 feature cells of about

319   similar cell volumes while the L1 is composed of smaller cells.

320

321   We then compared cell numbers between stages (Fig. 5E) and radial layers (Fig. 5F)

322   (Table 1). Overall, we observed a steady increase in cell numbers during primordium

323   outgrowth (Fig. 5E). The L1 covers a larger surface of the primordium than the L2 or L3.

324   Considering this aspect and given the smaller cell volume of L1 cells in comparison to

325   L2/L3 cells, we hypothesized that the L1 consists of more cells than the L2 and L3. This

326   assumption was supported by layer-specific cell counts (Fig. 5F) (Table 1). We also

327   determined that the L1 showed the largest percentage increase in cell numbers while the

328   L3 showed the least percentage increase in cell numbers (Fig. 5G).

329

330   Next, we assessed the spatial distribution of mitoses. To this end we manually labelled

331   cells that exhibit mitotic figures (Fig. 5A,B). We identified a total of 52 mitotic cells in

332   our dataset comprising 52 3D digital ovule primordia. We first asked if there were

333   differences in the number of mitoses between the cell layers. We found 33 mitotic cells in

334   the L1, 18 in the L2, and 1 in the L3. This result is in line with the observed differences in

335   cell numbers between the three layers (Fig. 5F). We then investigated if there was a

336   difference between the number of mitotic cells in the anterior and posterior L1. We found

337   23 and 10 mitoses in the anterior and posterior L1, respectively, indicating that more cell

338   divisions occur in the anterior domain. Finally, we analysed the proximal-distal

339   distribution of mitoses. We found that about 80 to 85 percent of scored mitotic cells were

340   located in the proximal half of the developing primordium (Fig. 5H).

341

342   Taken together, our data indicate that primordium outgrowth is preferentially driven by

343   an increase in cell number, not cell volume. In addition, they suggest unequal spatial

344   distribution of mitoses between cell layers and along the anterior-posterior and proximal-

345   distal axes. A higher number of mitoses in the anterior domain might explain primordium

346   slanting. The data further indicate that a cell proliferation zone located in the bottom half

347   of the developing primordium contributes significantly to its outgrowth.

348

349   **Funiculus curvature correlates with differences in cell number**

350   **and cell volume along the anterior-posterior and proximal-**

351   **distal axes**

352   To obtain insight into the cellular processes underlying funiculus curvature we performed

353   an initial analysis of its cellular characteristics using 14 3D digital ovules of stage 3-IV

14

354   (Fig. 6A-E). By this stage growth of the funiculus has ceased [27]. We focused on the L1

355   and L2 layers. To investigate cellular features of the L2 we digitally removed the L1 from

356   the 3D digital funiculi. First, we assessed the proximal-distal distance and cell number

357   along the L1 midlines of the anterior and posterior domains, respectively (Fig. 6A-E). We

358   observed that the anterior midline was longer and characterized by a higher number of

359   cells in comparison to the posterior midline. To directly compare volumes of anterior and

360   posterior cells we converted the cells' coordinates into relative proximal-distal positions

361   [53]. There we noticed a gradient in the volume of anterior L1 and L2 cells with the

362   distal-most cells featuring nearly 1.5 to 2 times the volume of cells located at the

363   proximal end (Fig. 6D,E). We did not detect a noticeable volume increase in the posterior

364   cells.

365

366   In summary, our data suggest that a combination of differential cell proliferation along

367   the anterior-posterior axis and unequal cell growth along the proximal-distal axis of the

368   anterior domain contributes to the curvature of the funiculus.

369

370   Proximal-distal growth gradient in Arabidopsis integuments

371   Genetic data indicated that asymmetric growth of the outer integument contributes

372   significantly to the anatropous shape of the ovule [27,54,55]. However, the 3D

373   architecture of integument cells in relation to their position within the tissue remained

374   unknown. Thus, we undertook a first analysis of the 3D geometry of integument cells in

375   3D digital ovules of stage 3-IV. At this stage curvature is underway but not yet

376   completed. We used 3DCoordX to measure cell volumes of the outer layer of the outer

377   integument along the proximal-distal axis. We found a gradient in cell volume along this

378   axis. We observed that proximal cells exhibited small cell volumes while, with the

15

379   exception of small cells at the tip of the integument, distal cells were characterized by

380   larger sizes (Fig. 7A). Next, we expanded the 3D cellular analysis to all cells of the

381   integuments. In a typical stage 3-IV 3D digital ovule we found a proximal-distal gradient

382   of cell volumes in cells of the other layers, but at a smaller scale compared to the outer

383   layer of the outer integument (Fig. 7A-C). We then compared cell length to cell position

384   along the proximal-distal axis in the medial domain of the inner layer of the outer

385   integument across five different specimens. We found that cell length increased along the

386   proximal-distal axis (Fig. 7D).

387

388   Taken together, our data suggest that preferential cell elongation along the proximal-distal

389   axis may be an important factor underlying differential growth of the outer integument

390   and ovule curvature.

391

392   Application to other plant organs

393   Finally, we explored if our approach for an organ-intrinsic coordinate system was useful

394   beyond the Arabidopsis ovule and could be of value to provide spatial context to cellular

395   growth patterns in different organs of various plant species. To this end we investigated

396   3D digital plant organs of diverse morphological complexity. We first inspected the

397   archegonium of the liverwort genetic model system *Marchantia polymorpha*. The

398   archegonium is an organ of simple morphology consisting of two main tissues: the

399   spherical venter harboring the egg cell and the elongated neck through which the sperm

400   cell reaches the egg cell [56]. We generated two 3D digital archegonia: a younger

401   specimen A and an older specimen B. Both archegonia were imaged, 3D segmented, and

402   cells of the neck, neck canal, venter, and venter canal were identified and labelled

403   manually. We removed the egg and canal cells from our analysis and focused on the

16

404   venters and the necks of the two 3D digital archegonia (Fig. 8A,B). A first inspection

405   already revealed differences between the two specimens. We observed that the venter of

406   specimen A possessed only one cell layer with no obvious signs of periclinal cell

407   division. By contrast, we found that a scattered pattern of periclinal cell divisions had

408   occurred in the venter of specimen B associated with the formation of a second cell layer

409   (Fig. 8B) [56]. This observation indicated temporal and spatial asynchrony in the control

410   of these periclinal cell divisions.

411

412   A monolayer of cells formed the necks of both specimens. We implemented an organ

413   coordinate system to enable a spatial analysis of some basic cellular parameters along the

414   long axes of the two specimens. We placed a Bezier ring at the boundary between the

415   venter and neck cells (Fig. 8A,B). The placement of the ring resulted in the assignment of

416   positive and negative organ coordinate values for the venter and neck cells, respectively.

417   We then assessed the basis of the differences in neck lengths between the two specimens.

418   Measuring neck length along the main central axis revealed that the neck of specimen B

419   was about 2 times longer than specimen A (329 µm versus 160 µm). We then asked if the

420   length disparity between the necks of the two specimens was due to a difference in cell

421   numbers and/or cell elongation. We determined 98 and 114 neck cells for specimens A

422   and B, respectively, indicating a minor difference in neck cell numbers. Next, we

423   quantified cell length along the central organ axis for all neck cells. We observed that the

424   neck cells of specimen A had an average length of 10.3 µm ± 2.4 µm and exhibited a

425   relatively uniform cell length (Fig. 8C). Neck cells of specimen B showed a more

426   heterogeneous distribution of cell length and were noticeably more elongated with an

427   average cell length of 20.8 ± 5.6 µm. Moreover, cell elongation increased towards the tip

428   of the neck in specimen B while no such increase was observed for specimen A (Fig. 8D).

17

429   The results indicated that enhanced cell elongation along the central axis of the neck was

430   mainly associated with the increase in neck length in specimen B in comparison to

431   specimen A.

432

433   Finally, we turned our attention to a plant organ of complex 3D morphology. The cup-

434   shaped trap of the aquatic carnivorous plant *Utricularia gibba* represents a highly curved

435   3D leaf form [57,58]. Quantitative growth analysis at the tissue level combined with

436   computer modeling indicated that the complex shape transformations occurring during

437   trap development are associated with differential rates and orientations of growth [59,60].

438   However, a quantitative analysis of 3D cellular parameters had not been performed. To

439   obtain first insight into the cellular basis of the growth patterns shaping the Utricularia

440   trap we generated a 3D digital representation with cellular resolution of an intermediate-

441   stage trap collected 6 days after initiation [59]. By this stage an invagination in the near-

442   spherical young trap had occurred, followed by the formation of further folds and tissue

443   broadening, and resulting in the emergence of the interior trap door and threshold (Fig.

444   9A-C). We manually labelled the various tissues, including the abaxial and adaxial cells

445   of the wall, the threshold, and the combined trap door/palate domain, and distinguished

446   between medial and lateral domains of the adaxial and abaxial wall, respectively. To

447   define an origin of the distance coordinate system we placed an ellipsoid Bezier ring at

448   the boundary between the base of the threshold and the wall of the trap (Fig. 9D). We

449   then asked if there were position-related differences in cell volume in the epidermal

450   layers of the wall and threshold by analyzing epidermal cells located along the respective

451   midlines of the tissues (Fig. 9E-G). We observed that cell volume varied along the

452   measured distances. For example, we noticed a sudden increase in cell volume in an

453   interval from 240 μm to 320 μm for cells of the abaxial wall (Fig. 9F). This region

18

454   precedes a prominent kink in the abaxial wall (Fig. 9E). By contrast, cell volumes of the

455   adaxial wall dropped towards the end. The decrease in cell volume was likely associated

456   with the tapering of the adaxial wall that could be observed in this area. Volumes of

457   threshold cells positioned within a range of 80 to about 150 μm from the origin showed

458   relatively small volumes in comparison to the cells flanking this interval (Fig. 9G). The

459   80-150 μm zone corresponded to a section of the threshold which was only moderately

460   curved and provided a large surface exposed to the lumen of the trap (Fig. 9E). Taken

461   together, the data revealed spatial differences in cell volume for all three examined tissues

462   of this specimen and support the notion that differential cell growth contributes to the

463   morphogenesis of the Utricularia trap.

464

465

466 # Discussion

467   The generation of biological form can be explained in terms of growth oriented relative to

468   an organ-centric coordinate system [7,28,61]. To understand tissue morphogenesis it is

469   therefore essential to provide spatial context to the quantitative analysis of the molecular

470   and cellular networks that underlie the development of tissues and organs. It requires

471   robust methods that enable the objective assignment of position to individual cells in a

472   rapid and reliable manner. Here, we developed 3DCoordX, a collection of computational

473   tools that enable the assignment of organ-centric coordinate systems to several different

474   plant organs with complex shapes that were not accessible with previous methods. By

475   applying mathematically defined criteria for the annotation of cell position in 3D the tools

476   largely eliminate user-derived ambiguities in the cell annotation process. 3DCoordX is

477   implemented as an add-on to the open-source software MorphoGraphX [11,14] (preprint).

478   A detailed user guide can be found in the supplement. 3DCoordX enables quantitative

479   analyses of cellular features in their spatial context, in a rapid manner, and on a large

480   scale.

481

482   We took advantage of the recently made available 3D digital reference atlas of the

483   Arabidopsis ovule to develop generic conceptual and computational approaches that

484   enable the assignment of 3D coordinate systems to organs of simple as well as complex

485   curved morphology. Previous efforts, such as iRoCS [9] and 3DCellAtlas [10], relied on

486   externally imposed coordinate systems. The design of the strategies for the annotation of

487   cell position presented here is guided by intrinsic patterning processes and assign cell

488   distance in relation to organ-centric developmental axes. Such tissue polarity axes are

489   thought to play a central role in the spatial control of growth [28,62,63]. To accommodate

490   the particular architecture of the ovule we devised two 3D coordinate systems, one for the

491   main "trunk", the central proximal-distal axis consisting of the nucellus, chalaza and

492   funiculus, and one for the integuments. Both coordinate systems are based on similar

493   general principles. First, we distinguish between individual cell layers as in the L1 to L3

494   layers of the primordium or the adaxial-abaxial (dorso-ventral) cell layers of the two

495   integuments. Importantly, with the concept of "outside wall area ratio" 3DCoordX

496   embodies a new strategy for the classification of the radial layers. It does not rely on a

497   surface mesh for classification and thus is more versatile than other published methods.

498   Second, the cell layers then become subdivided into two domains: the anterior-posterior

499   domains of the trunk and the medial-lateral domains of the integument cell layers. Third,

500   subsequent assignment of a proximal-distal distance value to each cell is constricted by

501   these two prepatterns. For the placement of reference Bezier rings we took cues from the

502   localization of important developmental regulators, such as the presence of an auxin

503   maximum at the distal tip of the ovule primordium or the *CUC3* expression in the chalaza

504   [39–41,52]. As a result of the approach each cell is annotated in 3D with respect to the

505   radial and proximal-distal dimensions as well as to either an anterior-posterior or medial-

506   lateral axis. With the help of 3DCoordX we readily discovered previously unidentified

507   cellular growth patterns in the primordium and integuments. For example, our data

508   indicate a basal cell proliferation zone in the ovule primordium and suggest that

509   preferential cell proliferation in the anterior domain is important for primordium slanting.

510   Moreover, we obtained evidence that the increase in cell volume along the proximal-

511   distal axis of the outer integument, a tissue without radial symmetry, is mainly explained

512   by an increase in cell length.

513

514   Importantly, our work revealed that the respective principles can be successfully applied

515   to the establishment of coordinate systems for organs of varying degrees of

516   morphological complexity and the subsequent quantitative analysis of 3D cellular

517   parameters. We provided evidence for a preferential increase in cell length during axial

518   neck growth of the Marchantia archegonium. Moreover, we identified distinct cellular

519   patterns possibly associated with important morphological features of the intricately

520   folded *U. gibba* trap. These data reveal that 3DCoordX has broad applicability and

521   eliminates the need to work with multiple different pipelines when analyzing the cellular

522   architecture of organs in 3D. The general strategies and computational methods put

523   forward in this work will greatly reduce the time required for the spatial analysis of

524   cellular parameters so central to various approaches, such as computational modeling of

525   morphogenesis or comparative morphometry of specimens from different genotypes.

526

527

528   ## Materials and Methods

Plant work and lines

Arabidopsis thaliana (L.) Heynh. var. Columbia (Col-0) was used as a wild-type strain.

Plants were grown on soil as described earlier [64]. The pKAN1::KAN1:2xGFP construct

[38] and the pCUC3::CFP line [52] were gifts from Marcus Heisler and Nicolas Arnaud,

respectively. Wild-type plants were transformed with the pKAN1::KAN1:2xGFP

construct using Agrobacterium strain GV3101/pMP90 [65] and the floral dip method

[66]. Transgenic T1 plants were selected on Glufosinate (Basta) (10 μg/ml) plates and

transferred to soil for further inspection. *Marchantia polymorpha* of the BoGa ecotype

was grown on half-strength Gamborg's B5 medium under long day conditions (16L:8D)

at 22°C. For induction of reproductive structures, plants were grown under 60 μmol white

light supplemented with far red light (730 nm) on half-strength Gamborg's B5 medium

supplemented with 1 % glucose and 14 g/L agarose [67]. Gametangiophores appeared

after 4–6 weeks.

Clearing and staining of tissue samples

Treatment of ovules of the pKAN1::KAN1:2xGFP and the pCUC3::CFP lines was done

as described in [68] and [27]. Tissue was fixed in 4% paraformaldehyde in PBS followed

by two washes in PBS before transfer into the ClearSee solution (xylitol (10%, w/v),

sodium deoxycholate (15%, w/v), urea (25%, w/v), in H2O) [69]. Clearing was done at

least overnight or for up to two to three days. Cell wall staining with SR2200

(Renaissance Chemicals, Selby, UK) was performed as described in [70]. Cleared tissue

was washed in PBS and then put into a PBS solution containing 0.1% SR2200 and a

1/1000 dilution of the nuclear stain TO-PRO-3 iodide (Thermo Fisher Scientific) for 20

minutes. Tissue was washed in PBS for one minute, transferred again to ClearSee for 20

minutes before mounting in Vectashield antifade agent (Vector Laboratories, Burlingame,

554　CA, USA). Marchantia archegoniophores were fixed for 1 week in 4% paraformaldehyde

555　in PBS followed by two washes in PBS before transfer to ClearSee. Clearing was done

556　for 4-7 days. Cell wall staining and subsequent clearing, washing and mounting steps

557　were the same as for Arabidopsis ovules. Archegonia were dissected in Vectashield

558　mounting medium (Vector Laboratories, Burlingame, CA, USA).

559

Microscopy and image acquisition

561　Confocal laser scanning microscopy of ovules stained with SR2200 and TO-PRO-3

562　iodide was performed on an upright Leica TCS SP8 X WLL2 HyVolution 2 (Leica

563　Microsystems) equipped with GaAsP (HyD) detectors and a 63x glycerol objective (HC

564　PL anterior-posteriorO CS2 63x/1.30 GLYC, CORR CS2). Scan speed was at 400 Hz, the

565　pinhole was set to 0.6 Airy units, line average between 2 and 4, and the digital zoom

566　between 1 and 2. For z-stacks, 12-bit images were captured at a slice interval of 0.24 μm

567　with voxel size of 0.125 μm x 0.125 μm x 0.24 μm. Laser power or gain was adjusted for

568　z compensation to obtain an optimal z-stack. Images were adjusted for color and contrast

569　using Adobe Photoshop 2021 (Adobe, San Jose, USA) or MorphographX [14] software.

570　Image acquisition parameters for the pKAN1::KAN1:2xGFP line were the following:

571　SR2200; 405 diode laser 0.10%, HyD 420–480 nm, detector gain 10. 2xGFP; 488 nm

572　Argon laser 2%, HyD 525-550 nm, detector gain 100. TO-PRO-3; 642 nm White Laser

573　2%, HyD 660–720 nm, detector gain 100. In each case sequential scanning was

574　performed to avoid crosstalk between the spectra. Image acquisition parameters for the

575　pCUC3::CFP line were the following: SR2200; 405 diode laser 0.10%, HyD 420–480

576　nm, detector gain 10. CFP; 514 nm Argon laser 2%, HyD 525-550 nm, detector gain 100.

577　TO-PRO-3; 642 nm White Laser 2%, HyD 660–720 nm, detector gain 100. In each case

578　sequential scanning was performed to avoid crosstalk between the spectra. Imaging

579   conditions for the Marchantia archegonia stained with SR2200 and TO-PRO-3 iodide

580   were the same as for the ovules. The late stage Marchantia archegonium was imaged

581   using the same 63x glycerol objective and a tilescan of 8 tiles. For z-stacks of the older

582   specimen, 8-bit images were captured at a slice interval of 0.33 μm with voxel size of

583   0.126 μm x 0.126 μm x 0.33 μm; for z-stack of the younger 12-bit images were captured

584   at a slice interval of 0.33 μm with voxel size of 0.127 μm x 0.127 μm x 0.33 μm. Tiles

585   were stitched and merged to form the final 3D image stack of the organ in Leica

586   Application Suite X data processing software (LASX v3.5.7.23225). The early stage

587   archegonium was imaged without tile scan.

588

589

Datasets and 3D cell segmentation

591   The dataset encompassing the segmented wild-type 3D digital ovules was described

592   earlier [27]. The two z-stacks of Marchantia archegonia were 3D cell segmented using the

593   PlantSeg pipeline [17]. The z-stack of the *Utricularia gibba* trap was obtained from a

594   fixed and modified pseudo-Schiff-stained [71] specimen [59]. 3D cell segmentation was

595   performed using the PlantSeg-MorphoGraphX hybrid method as described in [27]. In all

596   instances generation of cell surface meshes and cell type labeling was performed with

597   MorphoGraphX.

598

Software

600   The MorphographX software was used for the generation of cell surface meshes, cell type

601   labeling, and the analysis of 3D cellular features [14]. It can be downloaded from its

602   website (https://www.mpiz.mpg.de/MorphoGraphX). The 3DCoordX toolbox is

603   integrated as an add-on in MorphoGraphX 2.0. A detailed user manual is provided in the

24

604   supplement. The PlantSeg pipeline [17] was used for 3D cell boundary prediction and

605   segmentation. The software can be obtained from its Github repository

606   (https://github.com/hci-unihd/plant-seg).

607

Acknowledgements

620

Competing interests

622   There are no financial or non-financial competing interests.

623

Authors' contributions

625   AV, SS, RS and KS designed the study. AV, SS, RT, TAM, and KL performed the

626   experiments. AV, SS, RT, TAM, KL, MT, RS and KS interpreted the results. MT, RS and

25

629

References

631   1.   Boutros M, Heigwer F, Laufer C. Microscopy-based high-content
632   screening. Cell. 2015;163: 1314–1325.

633   2.   Hong L, Dumond M, Zhu M, Tsugawa S, Li C-B, Boudaoud A, et al.
634   Heterogeneity and robustness in plant morphogenesis: from cells to organs. Annu
635   Rev Plant Biol. 2018;69: 469–495.

636   3.   Jackson MDB, Duran-Nebreda S, Kierzkowski D, Strauss S, Xu H,
637   Landrein B, et al. Global Topological Order Emerges through Local Mechanical
638   Control of Cell Divisions in the Arabidopsis Shoot Apical Meristem. Cell Syst.
639   2019;8: 53–65.e3.

640   4.   Kierzkowski D, Runions A, Vuolo F, Strauss S, Lymbouridou R, Routier-
641   Kierzkowska A-L, et al. A Growth-Based Framework for Leaf Shape Development
642   and Diversity. Cell. 2019;177: 1405–1418.e17.

643   5.   Kierzkowski D, Routier-Kierzkowska A-L. Cellular basis of growth in
644   plants: geometry matters. Curr Opin Plant Biol. 2019;47: 56–63.

645   6.   Sapala A, Runions A, Smith RS. Mechanics, geometry and genetics of
646   epidermal cell shape regulation: different pieces of the same puzzle. Curr Opin Plant
647   Biol. 2019;47: 1–8.

648   7.   Thompson DW. On Growth and Form. 2nd ed. Cambridge, UK:
649   Cambridge University Press; 1942.

650   8.   Hejnowicz Z. Trajectories of principal directions of growth, natural
651   coordinate system in growing plant organ. Acta Soc Bot Pol. 1984;53: 29–42.

652   9.   Schmidt T, Pasternak T, Liu K, Blein T, Aubry-Hivet D, Dovzhenko A, et
653   al. The iRoCS Toolbox--3D analysis of the plant root apical meristem at cellular
654   resolution. Plant J. 2014;77: 806–814.

655   10.   Montenegro-Johnson TD, Stamm P, Strauss S, Topham AT, Tsagris M,
656   Wood ATA, et al. Digital Single-Cell Analysis of Plant Organ Development Using
657   3DCellAtlas. Plant Cell. 2015;27: 1018–1033.

658   11.   Strauss S, Runions A, Lane B, Eschweiler D, Bajpai N, Trozzi N, et al.
659   MorphoGraphX 2.0: Providing context for biological image analysis with positional
660   information. bioRxiv. bioRxiv; 2021. doi:10.1101/2021.08.12.456042

661   12.   Fernandez R, Das P, Mirabet V, Moscardi E, Traas J, Verdeil J-L, et al.
662   Imaging plant growth in 4D: robust tissue reconstruction and lineaging at cell
663   resolution. Nat Methods. 2010;7: 547–553.

664   13.   Lowekamp BC, Chen DT, Ibáñez L, Blezek D. The design of SimpleITK.
665   Front Neuroinform. 2013;7: 45.

666   14.   Barbier de Reuille P, Routier-Kierzkowska A-L, Kierzkowski D, Bassel
667   GW, Schüpbach T, Tauriello G, et al. MorphoGraphX: A platform for quantifying
668   morphogenesis in 4D. Elife. 2015;4: 05864.

669   15.   Stegmaier J, Amat F, Lemon WC, McDole K, Wan Y, Teodoro G, et al.
670   Real-time three-dimensional cell segmentation in large-scale microscopy data of
671   developing embryos. Dev Cell. 2016;36: 225–240.

672   16.   Eschweiler D, Spina TV, Choudhury RC, Meyerowitz E, Cunha A,
673   Stegmaier J. CNN-based preprocessing to optimize watershed-based cell
674   segmentation in 3D confocal microscopy images. IEEE; 2019. pp. 223–227.

675   17.   Wolny A, Cerrone L, Vijayan A, Tofanelli R, Barro AV, Louveaux M, et
676   al. Accurate and versatile 3D segmentation of plant tissues at cellular resolution.
677   Elife. 2020;9. doi:10.7554/eLife.57613

678   18.   Bassel GW, Stamm P, Mosca G, Barbier de Reuille P, Gibbs DJ, Winter
679   R, et al. Mechanical constraints imposed by 3D cellular geometry and arrangement
680   modulate growth patterns in the Arabidopsis embryo. Proc Natl Acad Sci U S A.
681   2014;111: 8685–8690.

682   19.   Yoshida S, Barbier de Reuille P, Lane B, Bassel GW, Prusinkiewicz P,
683   Smith RS, et al. Genetic control of plant development by overriding a geometric
684   division rule. Dev Cell. 2014;29: 75–87.

685   20.   Lora J, Herrero M, Tucker MR, Hormaza JI. The transition from somatic
686   to germline identity shows conserved and specialized features during angiosperm
687   evolution. New Phytol. 2017;216: 495–509.

688   21.   Pasternak T, Haser T, Falk T, Ronneberger O, Palme K, Otten L. A 3D
689   digital atlas of the Nicotiana tabacum root tip and its use to investigate changes in
690   the root apical meristem induced by the Agrobacterium 6b oncogene. Plant J.
691   2017;92: 31–42.

692   22.   Montenegro-Johnson T, Strauss S, Jackson MDB, Walker L, Smith RS,
693   Bassel GW. 3DCellAtlas Meristem: a tool for the global cellular annotation of shoot
694   apical meristems. Plant Methods. 2019;15: 33.

695   23.   Graeff M, Rana S, Wendrich JR, Dorier J, Eekhout T, Fandino ACA, et al.
696   A morpho-transcriptomic map of brassinosteroid action in the *Arabidopsis* root.
697   Molecular Plant. 2021; 2021.03.30.437656.

698   24.   Hernandez-Lagana E, Mosca G, Mendocilla-Sato E, Pires N, Frey A,
699   Giraldo-Fonseca A, et al. Organ geometry channels reproductive cell fate in the
700   Arabidopsis ovule primordium. Elife. 2021;10. doi:10.7554/eLife.66031

25.   Refahi Y, Zardilis A, Michelin G, Wightman R, Leggio B, Legrand J, et al. A multiscale analysis of early flower development in Arabidopsis provides an integrated view of molecular regulation and growth control. Dev Cell. 2021;56: 540–556.e8.

26.   Silveira SR, Le Gloanec C, Gómez-Felipe A, Routier-Kierzkowska A-L, Kierzkowski D. Live-imaging provides an atlas of cellular growth dynamics in the stamen. Plant Physiol. 2021 [cited 5 Aug 2021]. doi:10.1093/plphys/kiab363

27.   Vijayan A, Tofanelli R, Strauss S, Cerrone L, Wolny A, Strohmeier J, et al. A digital 3D reference atlas reveals cellular growth patterns shaping the Arabidopsis ovule. Elife. 2021;10. doi:10.7554/eLife.63262

28.   Whitewoods CD, Coen E. Growth and development of three-dimensional plant form. Curr Biol. 2017;27: R910–R918.

29.   Bouman F. The ovule. Johri BM, editor. Embryology of Angiosperms. New York: Springer Verlag; 1984. pp. 123–157.

30.   Endress PK. Angiosperm ovules: diversity, development, evolution. Ann Bot. 2011;107: 1465–1489.

31.   Robinson-Beers K, Pruitt RE, Gasser CS. Ovule development in wild-type Arabidopsis and two female-sterile mutants. Plant Cell. 1992;4: 1237–1249.

32.   Schneitz K, Hülskamp M, Pruitt RE. Wild-type ovule development in Arabidopsis thaliana: a light microscope study of cleared whole-mount tissue. Plant J. 1995;7: 731–749.

33.   Jenik PD, Irish VF. Regulation of cell proliferation patterns by homeotic genes during Arabidopsis floral development. Development. 2000;127: 1267–1276.

34.   Satina S, Blakeslee AF, Avery AG. Demonstration of the three germ layers in the shoot apex of Datura by means of induced polyploidy in periclinal chimeras. Am J Bot. 1940;27: 895–905.

35.   Reiser L, Modrusan Z, Margossian L, Samach A, Ohad N, Haughn GW, et al. The BELL1 gene encodes a homeodomain protein involved in pattern formation in the Arabidopsis ovule primordium. Cell. 1995;83: 735–742.

36.   Gross-Hardt R, Lenhard M, Laux T. WUSCHEL signaling functions in interregional communication during Arabidopsis ovule development. Genes Dev. 2002;16: 1129–1138.

37.   Sieber P, Gheyselinck J, Gross-Hardt R, Laux T, Grossniklaus U, Schneitz K. Pattern formation during early ovule development in Arabidopsis thaliana. Dev Biol. 2004;273: 321–334.

38.   Caggiano MP, Yu X, Bhatia N, Larsson A, Ram H, Ohno CK, et al. Cell type boundaries organize plant development. Elife. 2017;6. doi:10.7554/eLife.27421

39.   Benková E, Michniewicz M, Sauer M, Teichmann T, Seifertová D,

739   Jürgens G, et al. Local, efflux-dependent auxin gradients as a common module for
740   plant organ formation. Cell. 2003;115: 591–602.

741   40.   Liao C-Y, Smet W, Brunoud G, Yoshida S, Vernoux T, Weijers D.
742   Reporters for sensitive and quantitative measurement of auxin response. Nat
743   Methods. 2015;12: 207–10, 2 p following 210.

744   41.   Kawamoto N, Del Carpio DP, Hofmann A, Mizuta Y, Kurihara D,
745   Higashiyama T, et al. A peptide pair coordinates regular ovule initiation patterns
746   with seed number and fruit size. Curr Biol. 2020;30: 4352–4361.e4.

747   42.   Bencivenga S, Simonini S, Benková E, Colombo L. The transcription
748   factors BEL1 and SPL are required for cytokinin and auxin signaling during ovule
749   development in Arabidopsis. Plant Cell. 2012;24: 2886–2897.

750   43.   Galbiati F, Sinha Roy D, Simonini S, Cucinotta M, Ceccato L, Cuesta C,
751   et al. An integrative model of the control of ovule primordia formation. Plant J.
752   2013;76: 446–455.

753   44.   Villanueva JM, Broadhvest J, Hauser BA, Meister RJ, Schneitz K, Gasser
754   CS. INNER NO OUTER regulates abaxial- adaxial patterning in Arabidopsis ovules.
755   Genes Dev. 1999;13: 3160–3169.

756   45.   McAbee JM, Hill TA, Skinner DJ, Izhaki A, Hauser BA, Meister RJ, et al.
757   ABERRANT TESTA SHAPE encodes a KANADI family member, linking polarity
758   determination to separation and growth of Arabidopsis ovule integuments. Plant J.
759   2006;46: 522–531.

760   46.   Kelley DR, Skinner DJ, Gasser CS. Roles of polarity determinants in ovule
761   development. Plant J. 2009;57: 1054–1064.

762   47.   Aida M, Ishida T, Fukaki H, Fujisawa H, Tasaka M. Genes involved in
763   organ separation in Arabidopsis: an analysis of the *cup-shaped cotyledon* mutant.
764   Plant Cell. 1997;9: 841–857.

765   48.   Ishida T, Aida M, Takada S, Tasaka M. Involvement of CUP-SHAPED
766   COTYLEDON genes in gynoecium and ovule development in Arabidopsis thaliana.
767   Plant Cell Physiol. 2000;41: 60–67.

768   49.   Takada S, Hibara K, Ishida T, Tasaka M. The CUP-SHAPED
769   COTYLEDON1 gene of Arabidopsis regulates shoot apical meristem formation.
770   Development. 2001;128: 1127–1135.

771   50.   Breuil-Broyer S, Morel P, de Almeida-Engler J, Coustham V, Negrutiu I,
772   Trehin C. High-resolution boundary analysis during *Arabidopsis thaliana* flower
773   development. Plant Journal. 2004;38: 182–192.

774   51.   Sieber P, Wellmer F, Gheyselinck J, Riechmann JL, Meyerowitz EM.
775   Redundancy and specialization among plant microRNAs: role of the MIR164 family
776   in developmental robustness. Development. 2007;134: 1051–1060.

777   52.   Gonçalves B, Hasson A, Belcram K, Cortizo M, Morin H, Nikovics K, et

778 al. A conserved role for CUP-SHAPED COTYLEDON genes during ovule
779 development. Plant J. 2015;83: 732–742.

780 53.   Zhang Z, Runions A, Mentink RA, Kierzkowski D, Karady M, Hashemi
781 B, et al. A WOX/auxin biosynthesis module controls growth to shape leaf form. Curr
782 Biol. 2020. doi:10.1016/j.cub.2020.09.037

783 54.   Baker SC, Robinson-Beers K, Villanueva JM, Gaiser JC, Gasser CS.
784 Interactions among genes regulating ovule development in. Genetics. 1997;145:
785 1109–1124.

786 55.   Schneitz K, Hülskamp M, Kopczak SD, Pruitt RE. Dissection of sexual
787 organ ontogenesis: a genetic analysis of ovule development in Arabidopsis thaliana.
788 Development. 1997;124: 1367–1376.

789 56.   Shimamura M. *Marchantia polymorpha*: taxonomy, phylogeny and
790 morphology of a model system. Plant Cell Physiol. 2016;57: 230–256.

791 57.   Płachno BJ, Adamec L, Kamińska I. Relationship between trap anatomy
792 and function in Australian carnivorous bladderworts (*Utricularia*) of the subgenus
793 *Polypompholyx*. Aquat Bot. 2015;120: 290–296.

794 58.   Reifenrath K, Theisen I, Schnitzler J, Porembski S, Barthlott W. Trap
795 architecture in carnivorous *Utricularia* (Lentibulariaceae). Flora - Morphology,
796 Distribution, Functional Ecology of Plants. 2006;201: 597–605.

797 59.   Lee KJI, Bushell C, Koide Y, Fozard JA, Piao C, Yu M, et al. Shaping of a
798 three-dimensional carnivorous trap through modulation of a planar growth
799 mechanism. PLoS Biol. 2019;17: e3000427.

800 60.   Whitewoods CD, Gonçalves B, Cheng J, Cui M, Kennaway R, Lee K, et
801 al. Evolution of carnivorous traps from planar leaves through simple shifts in gene
802 expression. Science. 2020;367: 91–96.

803 61.   Coen E, Rebocho AB. Resolving conflicts: modeling genetic control of
804 plant morphogenesis. Dev Cell. 2016;38: 579–583.

805 62.   Kennaway R, Coen E, Green A, Bangham A. Generation of diverse
806 biological forms through combinatorial interactions between tissue polarity and
807 growth. PLoS Comput Biol. 2011;7: e1002071.

808 63.   Kuhlemeier C, Timmermans MCP. The Sussex signal: insights into leaf
809 dorsiventrality. Development. 2016;143: 3230–3237.

810 64.   Fulton L, Batoux M, Vaddepalli P, Yadav RK, Busch W, Andersen SU, et
811 al. DETORQUEO, QUIRKY, and ZERZAUST represent novel components
812 involved in organ development mediated by the receptor-like kinase STRUBBELIG
813 in Arabidopsis thaliana. PLoS Genet. 2009;5: e1000355.

814 65.   Koncz C, Schell J. The promoter of TL-DNA gene 5 controls the tissue-
815 specific expression of chimaeric genes carried by a novel Agrobacterium binary
816 vector. Mol Gen Genet. 1986;204: 383–396.

817   66.   Clough SJ, Bent AF. Floral dip: a simplified method for Agrobacterium-
818   mediated transformation of Arabidopsis thaliana. Plant J. 1998;16: 735–743.

819   67.   Althoff F, Kopischke S, Zobell O, Ide K, Ishizaki K, Kohchi T, et al.
820   Comparison of the *MpEF1α* and *CaMV35* promoters for application in *Marchantia*
821   *polymorpha* overexpression studies. Transgenic Res. 2014;23: 235–244.

822   68.   Tofanelli R, Vijayan A, Scholz S, Schneitz K. Protocol for rapid clearing
823   and staining of fixed Arabidopsis ovules for improved imaging by confocal laser
824   scanning microscopy. Plant Methods. 2019;15: 120.

825   69.   Kurihara D, Mizuta Y, Sato Y, Higashiyama T. ClearSee: a rapid optical
826   clearing reagent for whole-plant fluorescence imaging. Development. 2015;142:
827   4168–4179.

828   70.   Musielak TJ, Schenkel L, Kolb M, Henschen A, Bayer M. A simple and
829   versatile cell wall staining protocol to study plant reproduction. Plant Reprod.
830   2015;28: 161–169.

831   71.   Truernit E, Bauby H, Dubreucq B, Grandjean O, Runions J, Barthélémy J,
832   et al. High-resolution whole-mount imaging of three-dimensional tissue organization
833   and gene expression enables the study of Phloem development and structure in
834   Arabidopsis. Plant Cell. 2008;20: 1494–1503.

835

836

837

Figure legends

839
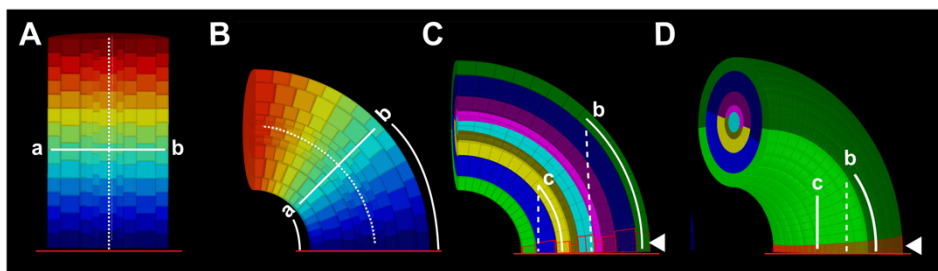
Fig 1. Axial cell distance determination in curved tissue. (A) Section through an

artificial template of a tube-like and straight tissue consisting of multiple concentric cell

layers. The heatmap indicates distance from the reference (red line at bottom). The

dashed line outlines the central axis. Note that the two cells (a,b) at the same cell index

845   position also show the same absolute axial distance to the origin (B) Same structure as in

846   (A) but curved. Note that cells a and b differ in their axial distances to the reference. (C)

847   Same structure as in (B). The separate cell layers are distinguished by their different

848   colors. Two cells in different layers are highlighted (c, b). Dashed lines indicate shortest

849   distances to the reference ignoring tissue layers. Solid lines mark the shortest distances to

850   the reference that are restricted to tissue layers. Confining the shortest distance to a given

851   layer reduces axial distance errors. The red line at the bottom highlights the reference.

852   The arrowhead marks origin cells outlined in red. Origin cells exhibit a close distance in

853   3D to the reference (5-15 μm). (D) 3D representation of (C) revealing how the anterior-

854   posterior boundary further minimizes the axial distance error for a cell in the posterior

855   half of the structure.

856

857
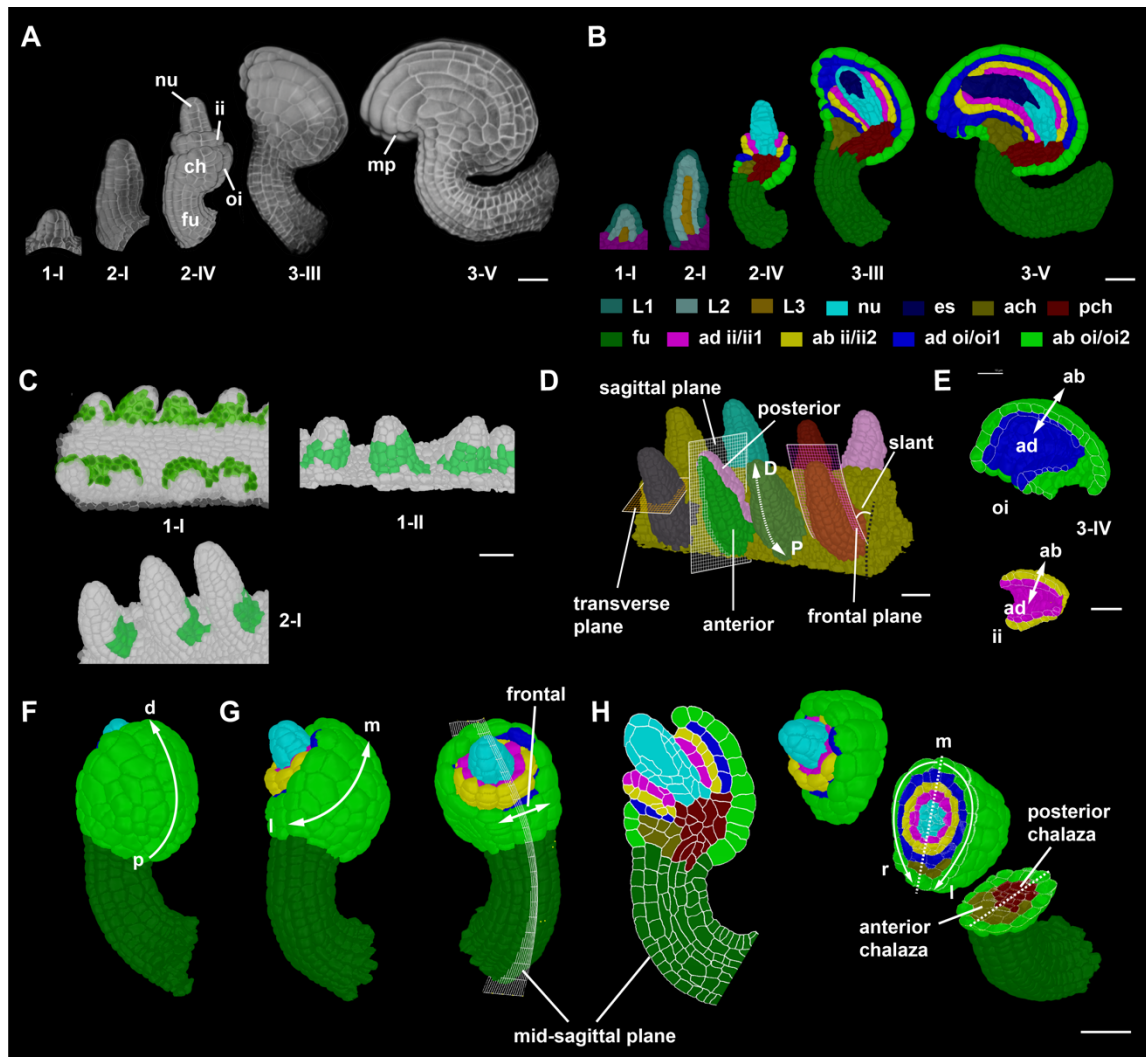
Fig 2. Developmental axes in ovule development. (A) 3D renderings of confocal z-stacks of SR2200-stained cell walls of wild-type ovules of the indicated stages. (B) Mid-sagittal sections through 3D digital ovules shown in (A). The different tissues are indicated. (C) 3D cell meshes highlighting the expression of the pKAN1::KAN1:2xGFP reporter in posterior epidermal cells from stage 1-I to 2-I in green. (D) 3D rendering of a placenta area carrying eight wild-type stage 2-I ovules. The anterior-posterior and proximal-distal axes are marked. The sagittal, transverse, and frontal planes are marked by grids on the primordia. Frontal plane separates the anterior and posterior halves of the organ. A Sagittal plane separates the left and right half of the organ. The dashed white arrow indicates the proximal-distal axis. Black dotted line indicates the placental surface

868 to which the posterior side of the ovule is slanted with a small angle. (E) Outer and inner

869 integument tissues extracted from the 3D mesh for visualizing the abaxial-adaxial

870 polarity. Tilted view of mid-sagittal sections through the outer and inner integument,

871 respectively, of a stage 3-IV 3D digital ovule. The arrows highlight the adaxial-abaxial

872 axes of each integument. (F) Posterior view of a stage 2-V 3D digital ovule with the

873 proximal-distal axis of the outer integument marked. (G) Side view (left) and anterior

874 view (right) of the 3D digital ovule shown in (F). The medial-lateral axis of the outer

875 integument and the frontal region are indicated. (H) A mid-sagittal section view (left) and

876 a 3D clipped view (right) of the 3D digital ovule shown in (F) is depicted. It is oriented

877 with the posterior side to the right. Tissue annotation as in (B). The 3D view allows the

878 discrimination of the left-right sides of the 3D digital ovule. The dashed line indicates the

879 medial line. Abbreviations: ab, abaxial; ad, adaxial; ach, anterior chalaza; ch, chalaza; ii,

880 inner integument; es, embryo sac; fu, funiculus; mp, micropyle; nu, nucellus; oi, outer

881 integument; pch, posterior chalaza; ml, medial-lateral; pd, proximal-distal; rl, right-left.

882 Scale bars: 20 μm.

883
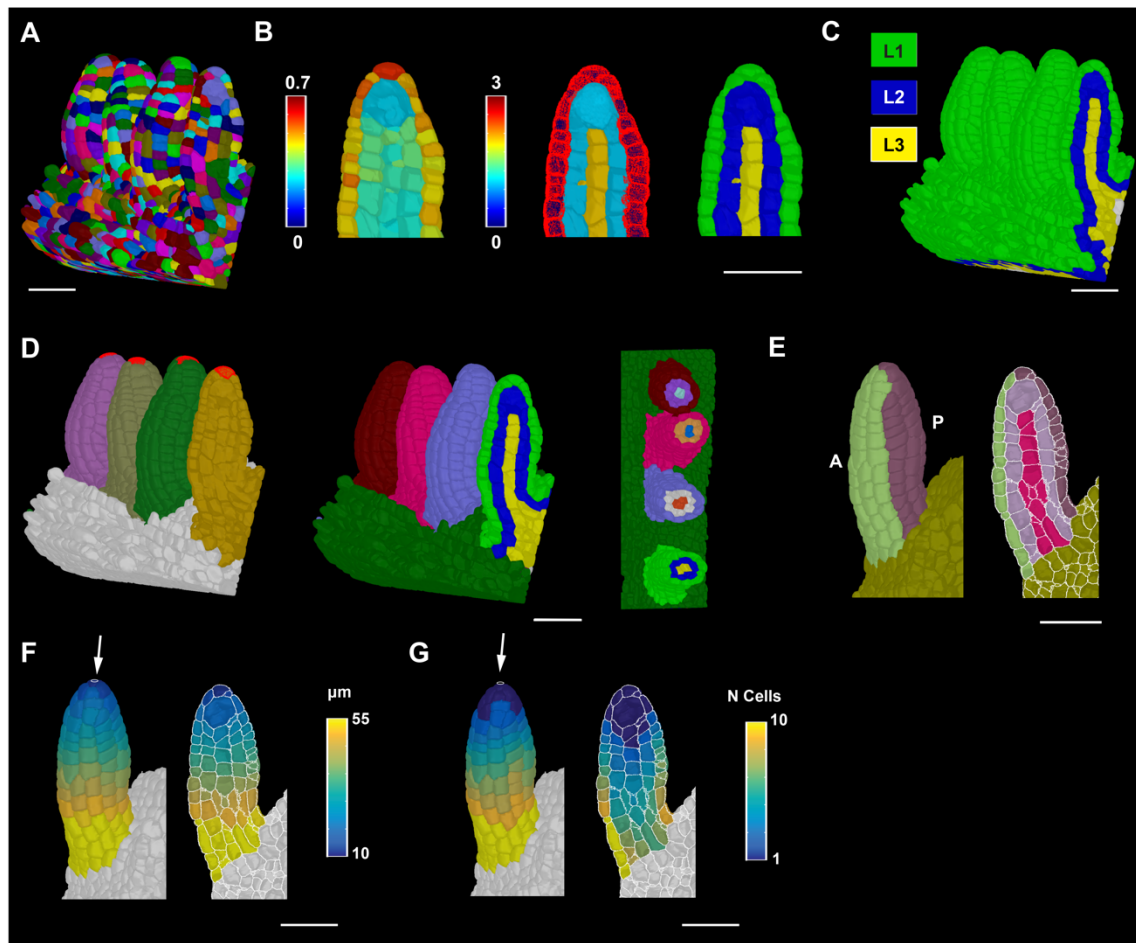
Fig 3. Ovule primordium tissue detection and coordinate system. (A) 3D segmented

cell mesh view of a pistil fragment with four ovules of late stage 2-I. (B) Left panel:

zoomed view of a sagittal section displaying the heatmap of outside wall area ratio.

Threshold selection of outer surface cells based on the heatmap of outside wall area ratio.

Center panel: heatmap indicates cell index, the number of cells an individual cell is

separated from the selected outer surface cells marked in red. Right panel: heatmaps of

cell distances (from center panel) were converted to integer values representing the tissue

identity labels L1, L2 and L3. (C) Same method applied to the entire 3D mesh shown in

(A). (D) Left panel: 3D Mesh view of the specimens shown in (A) with the distal most

cell selected for organ separation. Center panel: colors on individual ovule primordia

represent the results of organ separation after selecting the distal most cell and clustering

the cell connectivity network. Result of the combination of L1, L2 and L3 label and organ

897   separated labels annotated for the ovules shown in (A). Right panel: transverse section

898   displaying the L1, L2, L3 labels for different ovules in different colors. (E) Anterior and

899   posterior labels added to the tissue-annotated ovule primordia 3D cell meshes. Left panel:

900   surface view. Right panel: mid-sagittal section. (F) Heatmap of distance coordinates from

901   the point-like origin at the distal end of the organ (white arrow). Heat values indicate the

902   distance in μm from individual cells centroid to the Bezier ring (indicated by white arrow)

903   of the coordinates in a tissue restricted manner. Left panel: 3D view. Right panel: sagittal

904   section view. (G) Heatmap of cell coordinates instead of distance coordinates as in (F).

905   Heat values indicate how many cells apart is a cell of interest from the origin of the

906   coordinates through tissue-restricted manner. Left panel: 3D view. Right panel: sagittal

907   section view. Scale bars: 20 μm.

908

909
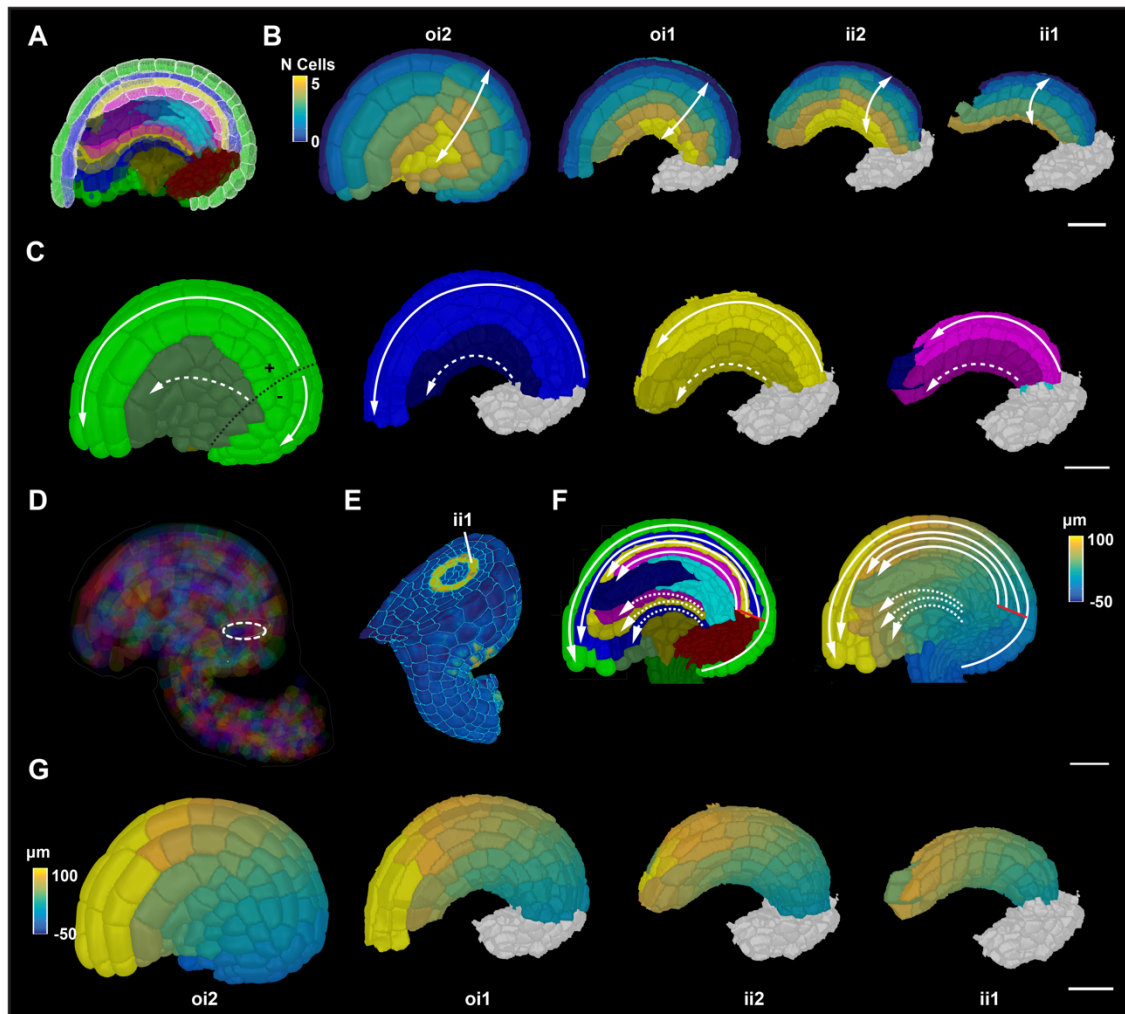
Fig 4. Integument coordinate system. (A) Mid-sagittal section highlighting the selected medial cells on the posterior side of the four layers of integument tissues for medial-lateral coordinate annotation. Colors represent tissue annotations similar to Fig. 1B. (B) Heatmap of medial-lateral cell coordinates. Heat values indicate the lateral position in terms of the number of cells from the median file of cells. Different integument tissues are extracted from the 3D mesh to display the medial-lateral coordinates at their tissue surface. (C) 3D surface view of integument tissues similar to (B). Medial and lateral cells are distinguished. Solid white line represents the tissue restricted coordinate direction along the medial group of cells. White dashed line represents the tissue restricted coordinate direction along the lateral group of cells. Black dotted line on oi2 represents the coordinate origin projected on the surface which separates the proximal oi2 cells with

921   negative coordinate values (D) Semi-transparent view of a mature 3D ovule displaying

922   the coordinate origin as a ring inside the organ. (E) 3D clipping view of a transverse

923   section of an ovule highlighting the ring-like expression of the pCUC3::CUC3:CFP

924   reporter in yellow. (F) Left panel: sagittal section of a mature ovule displaying the

925   coordinate directions of the medial and lateral group of cells in solid and white lines,

926   respectively. Solid red line indicates the origin of the coordinate system. Right panel:

927   Sagittal section displaying the heatmap of distance coordinates. Solid red line indicates

928   the origin of the coordinate system. (G) 3D surface view of integument tissues similar to

929   (B) displaying the distance coordinates at the surface of internal tissues. Scale bars: 20

930   μm.

931
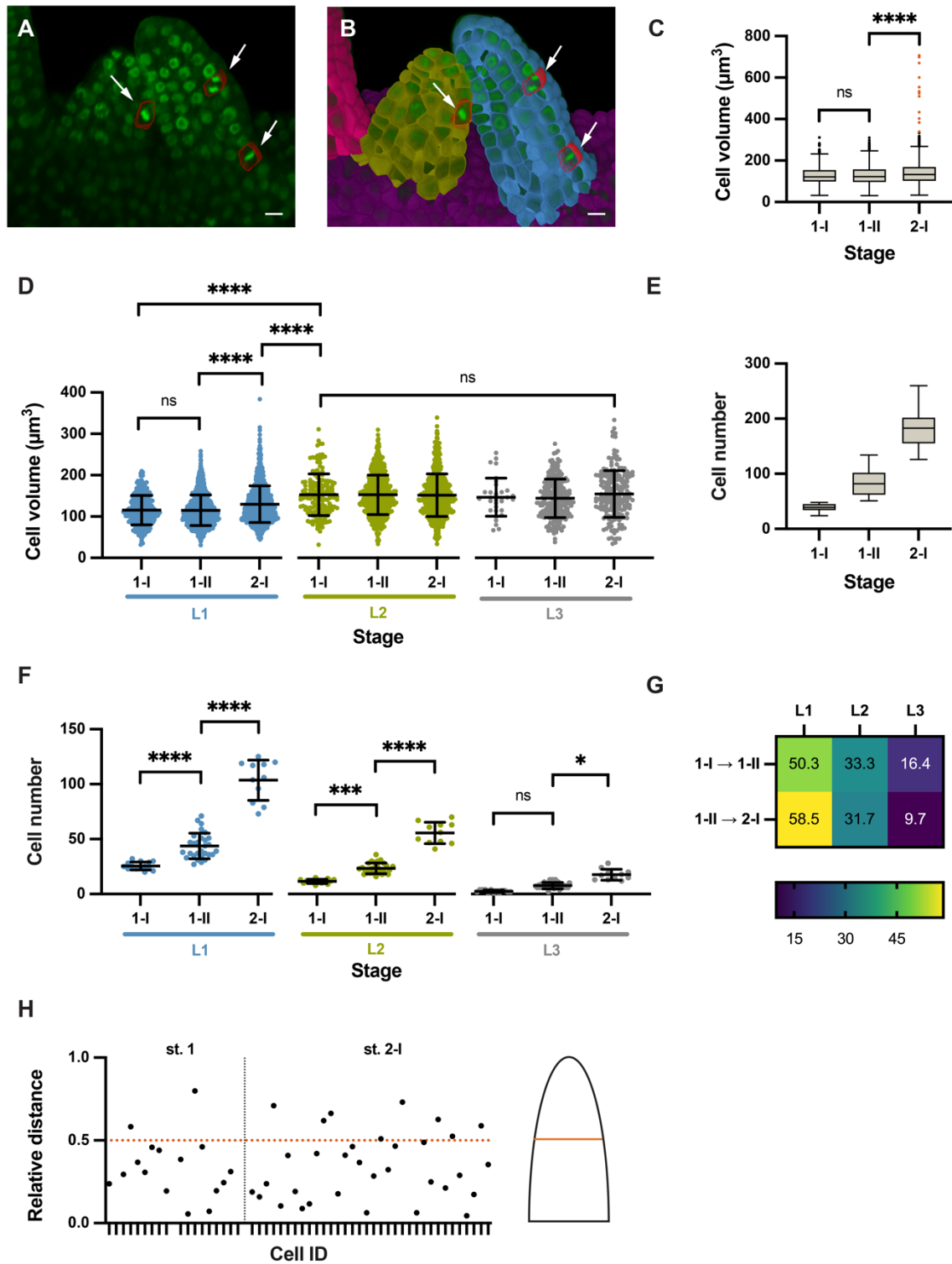
Fig 5. Cellular growth patterns in the ovule primordium. Different stages of wild-type (Col-0) ovule primordia are analyzed. (A) 3D frontal plane view of ovule primordia displaying the To-PRO-3 nuclear stain. Cells undergoing mitosis are outlined in red and marked by arrows. (B) Same section in (A) with an overlay of 3D labelled meshes.

937 Arrows indicate mitotic figures (C) Comparison of cell volumes. Box and whiskers plots

938 are shown. Whiskers extend to 1.5x the interquartile range from the 25 or 75 percentile,

939 respectively (Tukey). (D) Comparison of cell volume between radial layers of different

940 stages. (E) Comparison of cell numbers. Box and whiskers plots are shown. Whiskers

941 extend to 1.5x the interquartile range from the 25 or 75 percentiles, respectively (Tukey).

942 (F) Comparison of cell numbers between radial layers of different stages. (G) Heatmap of

943 percentage increase in number of cells per tissue compared to overall increase in number

944 of cells. (H) Plot showing the relative distance along the proximal-distal axis of mitotic

945 cells in a primordium. Relative distance was calculated by the following formula: reldist

946 = 1 - distance coordinate/mean length. The stages are indicated. Statistics in (D, F): data

947 are mean ± SD; significances: ****, $p < 0.0001$; ***, $p < 0.0004$; *, $p < 0.02$. Ordinary

948 one-way ANOVA followed by Tukey's multiple comparison test. Scale bars: 20 µm.

949
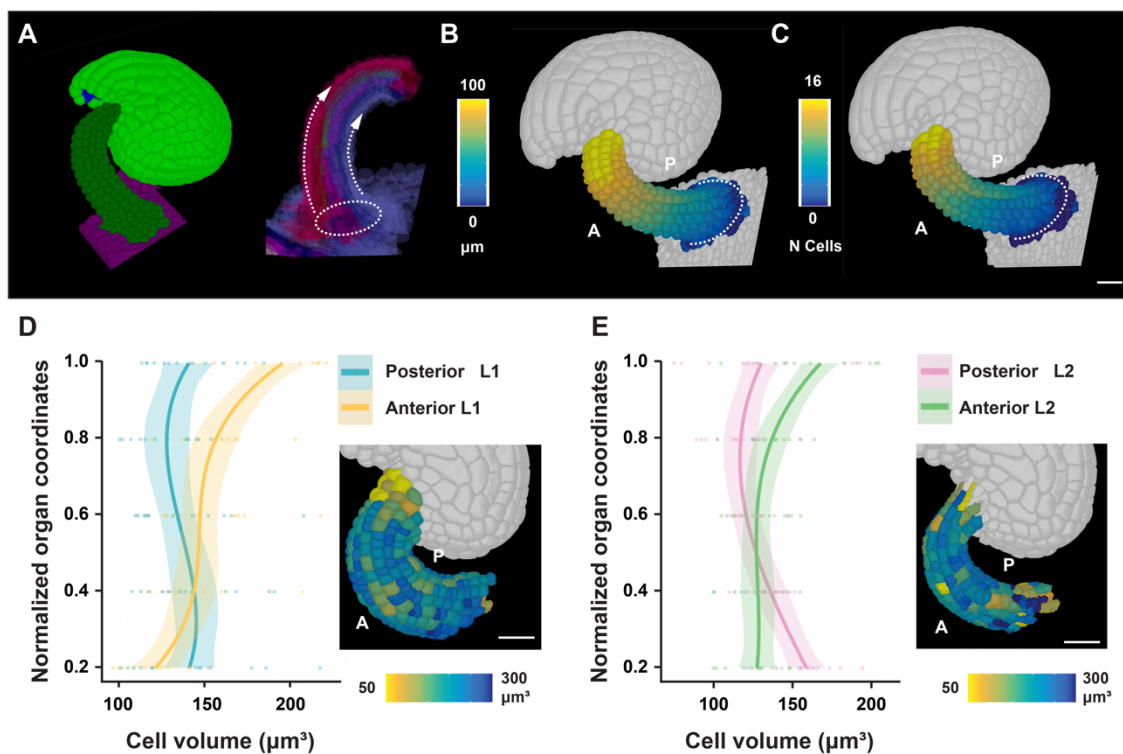
950

951   **Fig 6. Cellular features of funiculus curvature.** Wild-type (Col-0) ovules of stage 3-IV

952   are analyzed. (A) Left panel: Tilted side-view of a 3D cell mesh. Right panel: Semi-

953   transparent 3D mesh view of funiculus extracted from the 3D mesh of the organ. The

954   Bezier ring serving as origin is placed at the proximal base of the funiculus. The dashed

955   arrow lines indicate the coordinate direction along the anterior and posterior midlines.

956   (B,C) Same specimen as in (A). The anterior and posterior sides are marked. (B) Heatmap

957   of cell distances along the proximal-distal axis of the funiculus. (C) Heatmap of cell

958   numbers along the proximal-distal axis of the funiculus. White dotted line indicates the

959   coordinate origin as a ring. (D) Graph depicting cell volumes of anterior and posterior L1

960   cells in relation to the normalized proximal-distal position. The inset in the bottom right

961   corner shows a heat map of cell volume in the L1 of the funiculus. 14 3D digital ovules

962   were analyzed. Regression curves are cubic polynomials with 95% confidence intervals

963   (shaded regions)**.** Number of cells: $1568 \leq n \leq 1768$. (E) Similar graph as in (D) revealing

964   cell volumes of anterior and posterior L2 cells. Number of cells: $1175 \leq n \leq 1352$. Scale

965   bars: 20 μm.

966
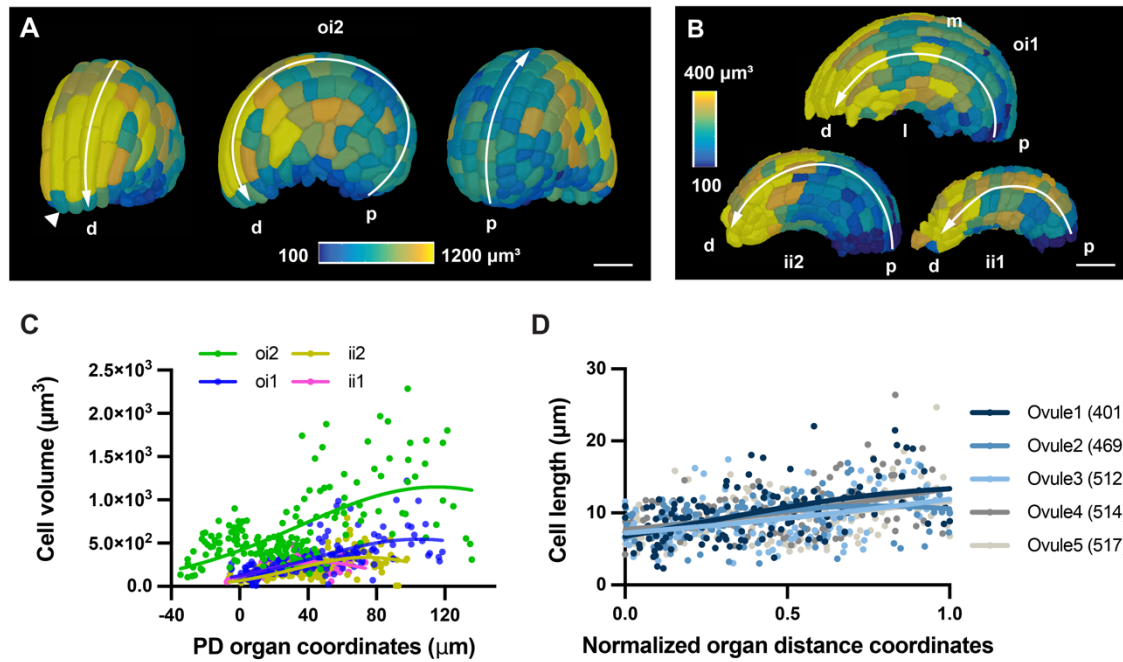
Fig 7. 3D geometry of integument cells. Wild-type (Col-0) ovules of stage 3-IV are analyzed. (A) Heatmap of oi2 cell volumes. Panels depict a tilted frontal view (left), side view (center), and tilted back view (right). The proximal-distal axis is indicated. The arrowhead marks a small tip cell. (B) Side views of the same specimen as in (A) showing the 3D surface view of internal tissues. Heatmaps of the oi1, ii2, and ii1 layers, respectively. (C) Graph showing cell volume in relation to proximal-distal distance for the four integument layers of a representative ovule. The respective nonlinear Gaussian regression curves are indicated. $95 \leq n \leq 172$. (D) Cell lengths in relation to normalized proximal-distal distance. Cells in the median oi1 layer of five ovules were analyzed. The respective nonlinear Gaussian regression curves are indicated. $126 \leq n \leq 133$. Note the increase in cell length towards the distal end. Abbreviations: d, distal; ii1, inner layer of inner integument; ii2, outer layer of inner integument; l, lateral; m, medial; oi1, inner layer of outer integument; oi2, outer layer of outer integument; p, proximal.Scale bars: (A,B) 20 μm.

42
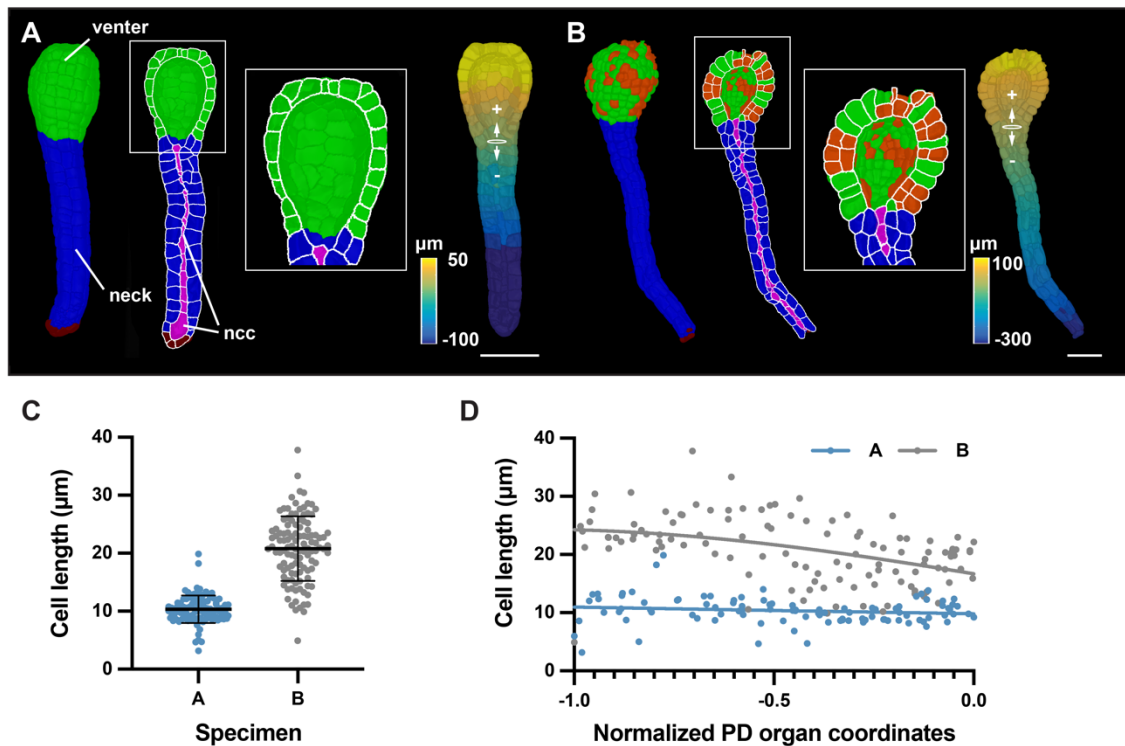
**Fig 8. Cellular analysis of 3D digital archegonia from Marchantia.** (A,B) 3D cell meshes of two different-stage archegonia are depicted. (A) Specimen A. The venter and neck are indicated. Left: 3D view. Center: An about mid-sagittal section. Right: Distance values along the central axis. The Bezier ring at the venter-neck boundary, which serves as the origin of the coordinate system, is indicated. (B) Specimen B. Identical arrangement as in (A). Highlighted white box represents the zoom view of the venter cells having undergone periclinal cell divisions marked in red. (C) Graph depicting the cell lengths of all neck cells of specimens A and B. The mean ± SD is indicated. Specimen A: n = 98. Specimen B: n = 114. (D) Graph showing cell length of individual neck cells of the two specimens shown in (C) in relation to their normalized position along the long axis of the neck. The tip of the neck is oriented to the left (0.0 corresponds to the ring position, the tip of the neck is at position -1.0, compare with Fig. 8B). Abbreviations: ncc, neck canal cells. Scale bars: (A,B) 50 μm.

43

998
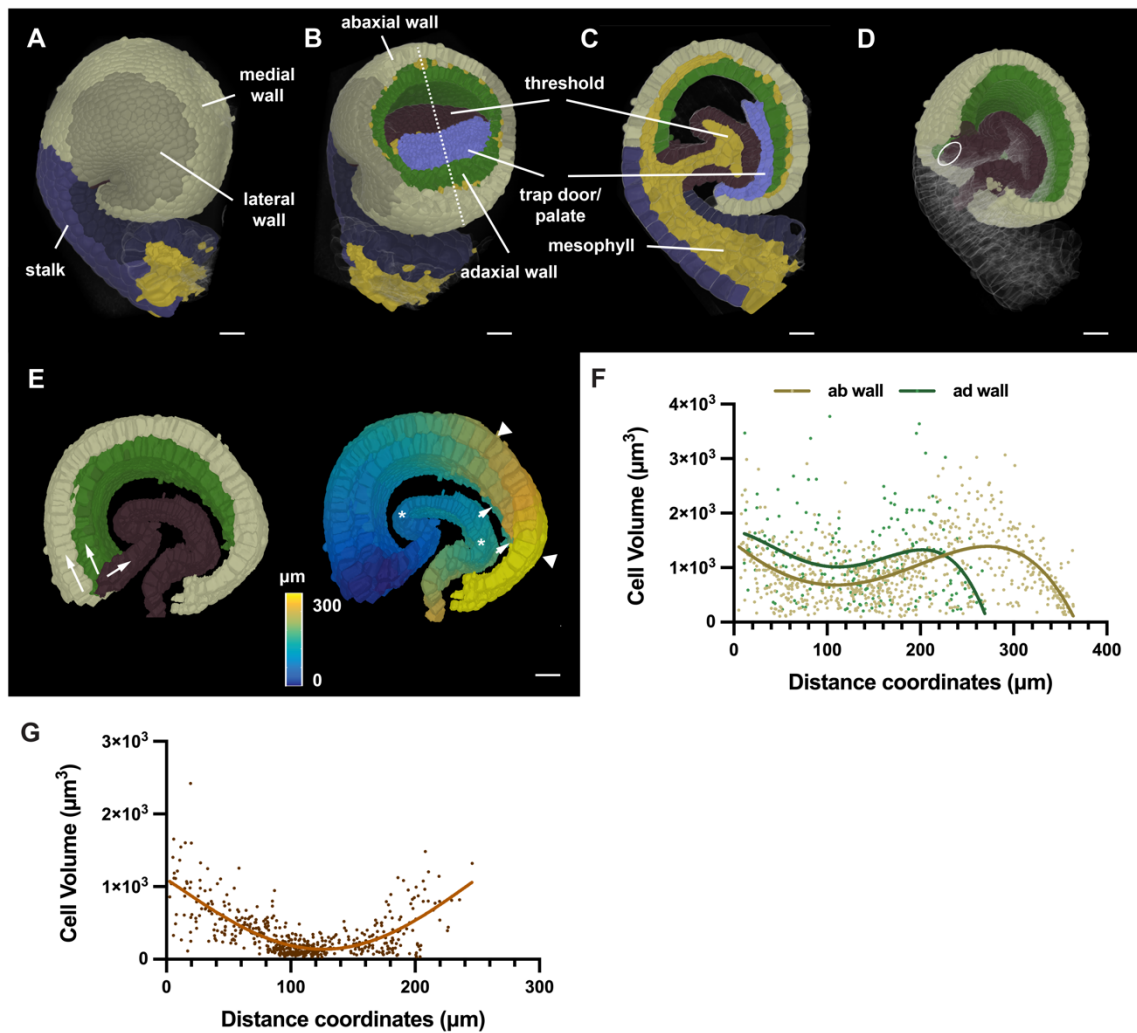
Fig 9. 3D digital Utricularia trap. A specimen 6 days after initiation is shown. (A) Side view of the 3D cell mesh with annotation of various tissues. (B) Tilted view of (A) with part of the wall removed by a tangential clipping plane. The dashed line indicates the mid-sagittal section shown in (C). (C) Mid-sagittal section. (D) Slanted 3D view of (A) with half of the trap cut off at the mid-sagittal plane shown in (B). The trap door and palate domain were removed. The position of the Bezier ellipsoid is indicated. (E) Left panel: arrows indicate the direction of the distance coordinates through the epidermis of the abaxial and adaxial tissue of the wall and the threshold, respectively. Right panel: Heat map indicating distances. Wall and threshold are treated separately. Triangles mark the 240-320 μm interval of the abaxial wall. Arrows highlight the tapering end of the adaxial wall. Asterisks indicate the 80-150 μm interval of the threshold. (F) Graph

44

1010   displaying cell volume of epidermal trap cells in relation to their position. Values for the

1011   abaxial and adaxial wall are superimposed. The respective nonlinear regression curves

1012   fitting a fourth order polynomial function are indicated. ab wall: n = 786, ad wall: n =

1013   231. (G). Graph displaying cell volume of threshold cells in relation to their position. The

1014   line marks a nonlinear regression curve. n = 533. Scale bars: 20 μm.

1015

Tables

1016

1017   **Table 1. Layer-specific cellular growth characteristics in the ovule primordium**

Cell layer	Stage[a]					
	I-I		1-II		2-I	
	Cell number	Cell volume[b]	Cell number	Cell volume[b]	Cell number	Cell volume[b]
L1	25.6 ± 3.7	115.6 ± 35.7	43.8 ± 11.6	115.2 ± 36.8	103.6 ± 18.4	129.9 ± 44.5
L2	11.6 ± 1.9	152.8 ± 50.3	23.4 ± 4.9	152.7 ± 47.6	55.6 ± 9.7	158.5 ± 74.2
L3	2.5 ± 1.2	146.8 ± 45.9	7.7 ± 2.8	144.1 ± 46.6	17.6 ± 5.0	154.7 ± 56.5

1018   [a]Number of 3D digital ovules scored: 14 (stage 1-I), 28 (stage 1-II), 11 (stage 2-I).

1019   [b]Volumes are given in μm^3.

1020   Values represent mean ± SD

The annotation and analysis of complex 3D plant organs using 3DCordX

Athul Vijayan[1,#a,¶], Soeren Strauss[2,¶], Rachele Tofanelli[1], Tejasvinee Atul Mody[1], Karen Lee[3], Miltos Tsiantis[2], Richard S. Smith[2,3] and Kay Schneitz[1,*]

[1]Plant Developmental Biology, TUM School of Life Sciences, Technical University of Munich, Freising, Germany

[2]Department of Comparative Developmental and Genetics, Max Planck Institute for Plant Breeding Research, Cologne, Germany

[3]The John Innes Centre, Norwich Research Park, Norwich, United Kingdom

[#a]Current address

Department of Comparative Developmental and Genetics, Max Planck Institute for Plant Breeding Research, Cologne, Germany
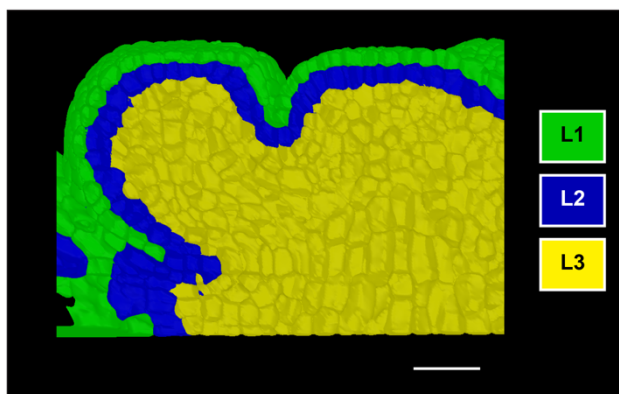
Fig S1. Automatic cell layer detection in the Arabidopsis shoot apical meristem. The outside wall area ratio approach was applied to automatically identify the three tissue layers. Layers are labelled with respective colors. Scale bar 20 μm.
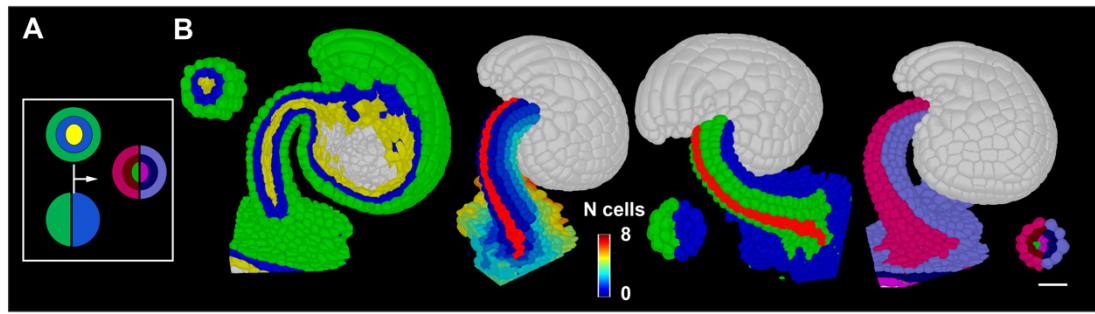
Fig. S2. Separation of funiculus into radial and anterior and posterior domains. A cartoon demonstrating the principle for the separation into radial L1, L2, L3 layers and anterior-posterior domains. (A) Results of L1, L2 and L3 tissue labels are combined with anterior and posterior labels to form the final tissue labels that separate individual radial layers and anterior-posterior tissues. (B) Figure demonstrating the step-by-step procedure for the detection of the anterior and posterior regions of the Arabidopsis funiculus. From left to right; first panel: L1, L2 and L3 labelled Arabidopsis ovule, a transverse section is shown at the top left; second panel: cells at roughly anterior midline are selected as origin (highlighted in red) and cell distance from these cells to other cells in funiculus are computed. Essentially the cell distance here represents the number of cells a cell is away from the anterior midline cells; third panel: the heatmap of cell distances from the second image is binned into two resulting in anterior and posterior tissue annotations; fourth panel: the results from first and third panel are merged to form the final tissue label that combines the information for L1, L2, L3 and anterior and posterior. This allows for example the distinction of anterior L1 and posterior L1 tissue. Scale bar 20 μm.